Int J CARS (2015) Volume 10, Issue 12, pp 1997–2007
(doi:10.1007/s11548-015-1233-y)

Multimodal Image-Guided Prostate Fusion Biopsy based on Automatic Deformable Registration

Oliver Zettinig · Amit Shah · Christoph Hennersperger · Matthias Eiber · Christine Kroll · Hubert Kübler · Tobias Maurer · Fausto Milletarì · Julia Rackerseder · Christian Schulte zu Berge · Enno Storz · Benjamin Frisch · Nassir Navab

Received: 23 March 2015 / Accepted: 29 May 2015

Abstract *Purpose.* Trans-rectal ultrasound (TRUS) guided random prostate biopsy is, in spite of its low sensitivity, the gold standard for the diagnosis of prostate cancer. The recent advent of PET imaging using a novel dedicated radiotracer, ^{68}Ga-labeled PSMA (Prostate Specific Membrane Antigen), combined with MRI provides improved pre-interventional identification of suspicious areas. This work proposes a multimodal fusion image-guided biopsy framework that combines PET-MRI images with TRUS, using automatic segmentation and registration, and offering real-time guidance. *Methods.* The prostate TRUS images are automatically segmented with a Hough transform based random forest approach. The registration is based on the Coherent Point Drift algorithm to align surfaces elastically and to propagate the deformation field calculated from thin plate splines to the whole gland. *Results.* The method, which has minimal requirements and temporal overhead in the existing clinical workflow, is evaluated in terms of surface distance and landmark registration error with respect to the clinical ground truth. Evaluations on agar-gelatin phantoms and clinical data of 13 patients confirm the validity of this approach. *Conclusion.* The system is able to successfully map suspicious regions from PET/MRI to the interventional TRUS image.

Oliver Zettinig, Amit Shah, Christoph Hennersperger, Christine Kroll, Fausto Milletarì, Julia Rackerseder, Christian Schulte zu Berge, Benjamin Frisch
Computer Aided Medical Procedures, Technische Universität München
Boltzmannstr. 3, 85748 Garching, Germany
Tel.: +49 (0)89 289 17079, E-mail: oliver.zettinig@tum.de

Hubert Kübler, Tobias Maurer, Enno Storz
Urologische Klinik und Poliklinik, Technische Universität München, Germany

Matthias Eiber
Nuklearmedizinische Klinik und Poliklinik, Technische Universität München, Germany

Nassir Navab
Computer Aided Medical Procedures, Technische Universität München, Germany and Johns Hopkins University, Baltimore, MD, USA

Keywords Prostate Biopsy · Multimodal Deformable Registration · Hough Forest Segmentation · Coherent Point Drift

1 Introduction

1.1 Prostate Cancer and Role of Imaging in Diagnosis

The current gold standard for the diagnosis of prostate cancer is a systematic 10 to 12 core random biopsy under trans-rectal ultrasound (TRUS) guidance [1]. Although TRUS provides live anatomical guidance, its poor detection of suspicious areas leads to a high rate of false negative results [29]. In contrast, MRI and PET are well-suited for the pre-interventional identification of suspicious regions by combining excellent anatomical soft-tissue contrast with metabolic information [29]. Recent studies report that combined MRI/TRUS image-guided biopsy is more accurate in detecting cancerous lesions with a significant Gleason score than conventional TRUS-guided biopsy [2, 5, 14, 20, 28, 31]. PET/TRUS fusion for prostate biopsy guidance has generated only moderate interest due to the low specificity of currently available radiotracers like ^{11}C-acetate, ^{11}C-choline and ^{18}F-FDG [29]. With the introduction of ^{68}Ga labeled ligands of Prostate-Specific Membrane Antigen (PSMA), exhibiting almost exclusive expression in the prostate and increased expression in prostate cancer [6], PET/TRUS and PET/MRI/TRUS fusion gains increasing attention [15]. Its higher cost is leveraged by the possibility to avoid serial biopsies with unclear outcome. However, up to now the usage of PSMA-PET/MRI has not yet been implemented into a biopsy guidance system.

Main challenges for the development of a multimodal fusion image-guided prostate biopsy framework are time and space constraints during the procedure. In particular, cognitive fusion of these imaging modalities, i.e. the exclusively mental alignment of images presented side-by-side, is error prone, highly depends on the ability of the urologist to interpret MRI or PET images, and thus remains marginally useful [5]. Therefore, computer-aided approaches are of great interest. Algorithms for image segmentation and registration, however, need to be fast and sufficiently accurate to be applicable in daily clinical routine.

Currently, a variety of commercial solutions on the market offer fusion biopsy functionality to some degree, employing different tracking systems to determine the position of their US transducer in space and registration algorithms to perform manual or semi-automatic rigid or elastic registration between 3D TRUS and MRI. They are usually rather bulky, require several lengthy interactions by the urologist – in particular for the segmentation of the prostate – and are mostly limited in their overall accuracy. We refer the reader to the excellent review by Sonn et al. [26] for further details. Advanced research on fusion approaches for MRI and TRUS is further summarized by Sperling et al. [28].

Xu et al. [31] and Kaplan et al. [12] register MRI and TRUS by respectively finding rigid and affine transformations based on fiducials. Reynier et al. [24] register the point clouds from TRUS and MRI surfaces using first rigid and then elastic transformations, however without modeling the real organ deformations. Prostate surface-based registration models using thin plate spline basis functions are reported by Cool et al. [2] and Mitra et al. [17], both requiring manual interaction.

In the work by Narayanan et al. [19] for MRI to TRUS deformable surface registration, an adaptive focus deformable model in a prostate phantom is used. Sparks et al.[27] and Hu et al. [10] have presented probabilistic and statistical shape and motion models of the prostate in patient datasets. The authors of these methods achieved low registration errors but also face time constraints for an integration into the clinical routine due to the manual prostate segmentation.

A fully automatic segmentation method with clinically acceptable accuracy within permissible time limits is highly desired. In this context, Ghose et al. [8] review the extensive research on semi-automatic and automatic segmentation of the prostate from TRUS and MRI images. The main approaches in delineating prostate boundaries are contour-, shape- or region-based, and can be distinguished in supervised or unsupervised classification, as well as combinations of these. A recent study by Qui et al. [21] has reported promising segmentation results by using convex optimization with axial symmetry enforcement for 3D TRUS and MRI prostate images. However, the use of axial symmetry is a disputable assumption, especially in diseased prostate conditions.

1.2 Aim of the Study

The aim of this work is to present, to the best of our knowledge, the first system for TRUS-based multimodal prostate biopsy guidance using elastically registered PSMA-PET/MRI datasets implemented in the routine clinical workflow. It includes all necessary components to automatically i) acquire, process and segment TRUS images, as well as to ii) register them to pre-interventional MRI and PET images, and to iii) finally use the fused information of all modalities for image-guidance to perform targeted prostate biopsies. Its integration into the regular clinical workflow is possible as the system requires minimal user interaction and performs US acquisition, segmentation and registration in less than five minutes - the time allocated for the local anaesthetic to take effect.

Due to the multimodal nature of our biopsy guidance system, it becomes furthermore possible to not only employ TRUS, MRI, and PET information at the same time for more accurate lesion targeting but also to assess the diagnostic value of novel imaging modalities such as ^{68}Ga-PSMA-PET/MRI for detecting prostate carcinomas.

This study extends our previous work [25], where we presented an open-source, multimodal image-guided prostate biopsy framework for the research and validation of image computing methods, as follows:

i Instead of using a rigid registration based on landmarks manually selected immediately before the biopsy procedure, the presented system uses automatic TRUS segmentation based on machine learning techniques. In particular, we use a Hough forest approach that was successfully applied for the fully automatic segmentation of retrospective cardiac datasets [16].

ii We employ a deformable registration based on automatic segmentation and the Coherent Point Drift algorithm, allowing a better global overlay of the MRI and PET images onto the ultrasound image.

iii For quantitative evaluation of our automatic system, we report results on phantom and patient datasets and compare against expert annotations serving as ground truth data.

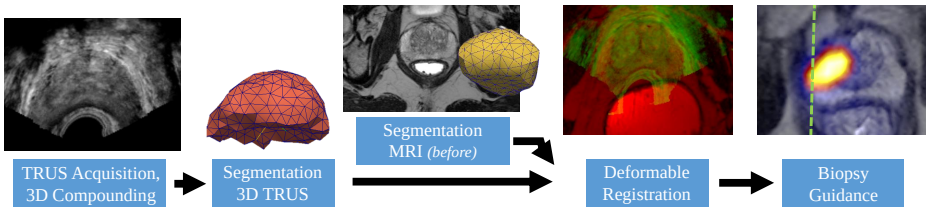

Fig. 1 Overview of the clinical protocol for multi-modal image-guided prostate biopsies. Apart from the MRI segmentation, which can be obtained in advance, all steps need to be performed within a time frame of around five minutes to fit into the time requirements of conventional, only US-guided biopsy procedures.

While the underlying algorithms used for segmentation and registration have already been presented in the literature, this work is the first to employ these algorithms with necessary modifications on the challenging prostate anatomy and present results of their performance, not only on image data but in their real application on phantoms and patients. In this work, the necessary components of our system and the employed algorithms are described in Sec. 2. After a validation of our method on agar-gelatin phantoms, the complete biopsy guidance system is analyzed on a dataset of 13 real patients. Finally, Sec. 4 concludes the paper.

2 Methods

The proposed multimodal prostate fusion biopsy system is embedded into the clinical routine as illustrated in Fig. 1. First, 2D TRUS images of the prostate are acquired and compounded into a 3D volume. Section 2.1 describes the components of the system as well as the image acquisition and compounding process. Next, the prostate is automatically segmented in TRUS using a Hough forest classifier, and a surface mesh is generated. The segmentation algorithm is detailed in Section 2.2. Thereafter, a modified version of the Coherent Point Drift algorithm [18] is employed to deformably register the surfaces of the MRI and TRUS segmentations, and warped versions of MRI and PET are computed using thin-plate splines, which is presented in Section 2.3. Finally, we present in Section 2.4 how the registered images are used for live prostate biopsy guidance.

2.1 System Components and Image Acquisition

Our system, as illustrated in Fig. 2, consists of three components [25]: an US system, a tracking system and a workstation. Firstly, we employ a conventional Hitachi AVIUS® US system with a 2D front fire trans-rectal probe (Model EUP-V53W) for image acquisition. This system is routinely used for US-guided prostate biopsies by attaching calibrated needle holders to the probe and following a needle guide on the US images. In this work, the US-based guidance is not altered but augmented with MRI and PET information.

Secondly, the US probe is tracked by an NDI Polaris® optical tracking system. The tracking target is rigidly attached opposite of the needle guide. An additional

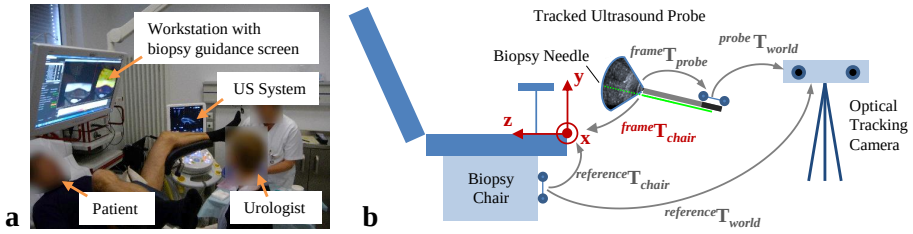

Fig. 2 a) System overview during the intervention. The urologist performing the prostate biopsy uses MRI and PET information in addition to the TRUS images on the US system for targeting suspicious lesions. **b)** Coordinate systems used to reconstruct a 3D TRUS volume in the coordinate system of the chair to make the initialization for MRI registration straightforward. *See text for details.*

reference tracking target is attached to the patient chair, allowing to move the tracking camera freely during the intervention (see Fig. 2b).

Finally, a workstation is required for image processing. We employ a system with 2 Intel Xeon® processors running at 2.13 GHz with 32GB RAM and an NVIDIA GeForce® GTX TITAN Black graphics card. Due to lack of access to RF data from the US machine, we use a StarTech frame grabber to acquire high resolution (1280×1024 pixel) digital images.

We utilize the open source software SlicerIGT[1] to perform spatial calibration of the US image to optical tracking (${}^{\text{frame}}\text{T}_{\text{probe}}$). Further, we use the freely available PLUS framework [13] for temporal calibration, tracked freehand US acquisition and for the compounding of 3D TRUS images [25]. For US compounding, linear interpolation and hole filling with the Gaussian accumulation technique available in PLUS is employed. Best performance of our system was achieved with an isotropic voxel spacing of 0.5 mm. Larger spacings incorporate more averaging artifacts, while smaller spacings only increase the segmentation time without any further improvement in its quality. The 3D volumes are embedded in the chair coordinate system, which is mapped to the 2D TRUS slices as follows (see Fig. 2b):

$$ {}^{\text{frame}}\text{T}_{\text{chair}} = {}^{\text{reference}}\text{T}_{\text{chair}} \cdot ({}^{\text{reference}}\text{T}_{\text{world}})^{-1} \cdot {}^{\text{probe}}\text{T}_{\text{world}} \cdot {}^{\text{frame}}\text{T}_{\text{probe}} \quad (1) $$

The usage of the chair coordinate system allows simple translational initialization of the subsequent registration step. Note that the patient is strictly told to remain static during the entire intervention.

2.2 Prostate Segmentation

A fully automatic prostate segmentation in compounded 3D TRUS volumes is obtained using Hough forests, a method coupling the classification performance of random forests with object localization capabilities. In our method, we further extend these with a strategy to extract a segmentation contour once the position of the prostate in the image is obtained through a voting strategy. The algorithm is

[1] Available online: `http://www.slicerigt.org`

similar to the one presented by Rematas et al. in [23], and is based on the technique presented in [16] already applied to the segmentation of 3D echocardiographic data.

Our Hough forest is an ensemble of Hough trees, trained on a set of TRUS volumes of various size and common spacing using segmentation contours, which were manually annotated by experts. During training, a grid of sampling points over each annotated volume is defined. Around each point, a 1,000-dimensional feature vector corresponding to the entire pattern of intensities in a $10 \times 10 \times 10$ pixel patch of the volume is extracted. We chose high dimensional feature vectors since we rely on the capabilities of the Hough forest to select the features that are most discriminative for the problem at hand [22].

The sampling-points belonging to a narrow region around the prostate boundary, denoted as foreground, are also associated with a vote $\mathbf{v}$, in the form of a displacement vector from the sampling point itself to the center of mass of the prostate. Additionally, the original position $\mathbf{p}$ in the training volume of each point of the foreground is stored and supplied to the training algorithm.

Training a Hough tree amounts to recursively splitting the training set T in the splitting nodes until one of the termination criteria is met, in which case the recursion is stopped and a leaf is instantiated. In our framework, the termination criteria are defined as a depth of 18 levels, or alternatively, a population smaller than 30 data points reaching a particular node. The splits are chosen such that either the information gain is maximized (Eq. 2) or the vote scattering (Eq. 3) is minimized. In the first equation, the splitting threshold θ is chosen such that the difference between the Shannon entropy of the splitting node $H(T)$ and the weighted Shannon entropies $H(T_l)$ and $H(T_r)$ of each of the child nodes is maximized. While this ensures good classification capabilities, Eq. 3 provides a criterion to choose the splitting threshold using only the votes $\mathbf{v}$ associated with data points $\mathbf{d}$ belonging to the foreground. The votes reaching each child node are compared in terms of squared distance to the mean vote for that child node. This measure is minimized to ensure minimal vote scattering after the split.

$$I(T,\theta) = H(T) - \sum_{T_i=\{T_l,T_r\}} \frac{|x \in T_i|}{|x \in T|} H(T_i) \tag{2}$$

$$V(T,\theta) = \sum_{k=\{l,r\}} \sum_{\mathbf{d}_i \in fg} (\mathbf{v}_i^k - \bar{\mathbf{v}}_k)^2 \tag{3}$$

Apart from the class posterior distribution, when a leaf is instantiated, we store one vote $\mathbf{v}_i$ and the original position of the data-point $\mathbf{p}_i$ for each data-point $\mathbf{d}_i$ belonging to the foreground and reaching that leaf.

During testing, an image that was not employed for training is sampled using a regular grid. The features of each data point are used to traverse each tree until reaching a leaf node. If a data point is classified as foreground by a sufficient number of trees in the forest, all the votes contained in the leaf nodes reached by this data point are weighted by the classification confidence and accumulated in a volume having the same dimensionality as the image. Additionally, as the votes are being cast, a pixel-wise reprojection list of votes is filled with information about the provenance of each vote and the position of the corresponding training data point in the ground truth images. The position where the maximum number of votes was attained represents the position of the prostate's center of mass in the test image.

Using the information stored in the reprojection list in the immediate neighbourhood of the maximum vote, we are then able to propagate portions of ground truth contours from the training images onto the newly acquired test image. Additionally, we weight each contribution by the truncated normalized cross correlation between the intensities of the currently considered patch $\mathbf{p}_i$ in the test image and the patch $\mathbf{p}_t$ of the training image:

$$NCC(\mathbf{p}_i, \mathbf{p}_t) = \max\left(\frac{1}{N}\sum \frac{(\mathbf{p}_i^i - \bar{\mathbf{p}}_i)(\mathbf{p}_t^i - \bar{\mathbf{p}}_t)}{\sigma_i \sigma_t}, 0\right). \tag{4}$$

After the reprojection is complete, a normalization step is performed in order to obtain a probabilistic segmentation, which can thereafter be thresholded at 0.5. We perform an automatic connected component analysis as post-processing, resulting in a precise delineation of the boundary of the prostate. Our implementation of the Hough forest algorithm is based on the Sherwood C++ library [3]. For subsequent registration, we finally employ the CGAL library[2] to triangulate the binary volumetric segmentation image and create a surface mesh.

2.3 Deformable Surface-based Registration

The previously generated surface meshes from the TRUS and MRI segmentations are now used to deformably register both images. Such a registration can be understood as a two-step process: Firstly, only the surface meshes are deformably registered, for instance by computing displacements for each vertex of one mesh such that a distance d between both meshes is minimized. Secondly, these sparse displacements are used to interpolate a dense deformation field over the entire image domain in order to warp the MRI image onto the TRUS image.

In this work, we achieve the first step, i.e. the mesh registration, by employing a modified version of the Coherent Point Drift (CPD) algorithm [18], which is a fully deformable point registration method without any geometrical constraints regarding the shapes to be registered. Additionally, it also shows robustness in terms of outliers as it forces the points to move coherently. The algorithm registers two sets of points, which are both modeled as centroids of Gaussian mixture models (GMMs). The first set of points $\mathrm{X} \in \mathbb{R}^{n\times 3}$ comprises the vertices of the TRUS mesh and is considered static. The vertices of the MRI mesh are collected in the second, moving set of points $\mathrm{Y} \in \mathbb{R}^{m\times 3}$, which is fitted to X during the registration procedure using expectation maximization (EM). m and n denote the number of points in the two sets, respectively. For numerical robustness, both point sets are demeaned and normalized with respect to translation and scale. The goal of the algorithm is now to find a non-rigid transformation $\mathcal{T}$ such that the deformed point set $\mathrm{Y}' = \mathcal{T}(\mathrm{Y}, v) = \mathrm{Y} + v(\mathrm{Y})$ is given as the initial positions plus an optimal displacement vector field v. Assuming that for a proper mesh registration the two Gaussian mixtures will be statistically similar, mesh vertex correspondences will be derived, expressed as the maximum of the GMM posterior probability for any given data point. Therefore, the L_2 distance is well suited as a cost function for the parameter optimization:

$$d_{L_2} = \int \left[\mathrm{gmm}(\mathcal{T}(\mathrm{Y}, v)) - \mathrm{gmm}(X)\right]^2 dx. \tag{5}$$

[2] Computational Geometry Algorithms Library, available online: `http://www.cgal.org`

In this notation, $\mathrm{gmm}(\mathcal{P}) = \sum \alpha \mathcal{N}(\mu, \Sigma)$ denotes the Gaussian mixture density of point set $\mathcal{P}$ with weights α. Our CPD implementation is based on the version of Jian and Vemuri [11][3] and uses thin-plate splines (TPS) as parametrization for $\mathcal{T}$. A TPS transformation can be decomposed into an affine as well as a non-linear part parametrized by a set of warping coefficients w. As such, the relation between the moving and the original MRI mesh vertices can be expressed as:

$$\mathrm{Y}' - \mathrm{Y} = \left[\mathrm{Y}|\mathbf{1}\right] \mathrm{A}^\intercal + \mathrm{U}\mathrm{w}. \tag{6}$$

Hereby, $\mathbf{1}$ is a column vector of size m. The matrix $\mathrm{A} \in \mathbb{R}^{3\times 4} = \left[\mathrm{B}|\mathbf{t}\right]$ models the affine part of the motion with translation $\mathbf{t}$, and rotation and scaling B. The basis matrix $\mathrm{U} \in \mathbb{R}^{m\times m}$ for the local, non-linear transformations is expressed using radial basis functions in 3D, i.e. $\mathrm{U} = \{u_{i,j}\}$, $u_{i,j} = \|\mathrm{Y}'_i - \mathrm{Y}_j\|$. It has been shown that efficient, gradient-based numerical optimization techniques are suited to solve for A and w [11], using the following discretized cost function $D_{L_2}(\mathrm{Y}')$ and its derivatives:

$$\begin{aligned} D_{L_2} &= \sum_{i=1}^{m}\sum_{j=1}^{n} p_{i,j} + \frac{\lambda}{2}\operatorname{tr}(\mathrm{w}^\intercal \mathrm{K}\mathrm{w}) \\ \frac{\partial D_{L_2}}{\partial \mathrm{A}} &= \left[\mathrm{Y}|\mathbf{1}\right]^\intercal \mathrm{G}, \qquad \frac{\partial D_{L_2}}{\partial \mathrm{w}} = \mathrm{U}^\intercal \mathrm{G} + \lambda \mathrm{K}\mathrm{w}. \end{aligned} \tag{7}$$

The matrix $\mathrm{P} \in \mathbb{R}^{m\times n} = \{p_{i,j}\}$, $p_{i,j} = \exp\left[-\|\mathrm{Y}_i - \mathrm{X}_j\|/(2\sigma^2)\right]$ includes the GMM posterior probabilities, and $\|\cdot\|_F$ denotes the Frobenius norm. For the optimization, the derivative matrix $\mathrm{G} \in \mathbb{R}^{m\times 3} = \partial D_{L_2}/\partial \mathrm{Y}'$ can be obtained using P. The regularization term with kernel matrix $\mathrm{K} \in \mathbb{R}^{m\times m} = \{k_{i,j}\}$, $k_{i,j} = \|\mathrm{Y}_i - \mathrm{Y}_j\|$ and weighting parameter λ impose penalties on the bending of the TPS deformation field.

As the parameters v are initialized with 0, the algorithm will intuitively first establish an affine transformation, which could cause significant rotation or shearing of the prostate meshes, and only then fine-tune the local non-rigid TPS components. However, minimal rotation is to be expected because the chair coordinate system (see Fig. 2b) is defined to match the orientation of the coordinate system of the MRI, and the translation should also be small because both point sets were demeaned before the registration. Therefore, we constrain the affine part to the identity transformation in the first k iterations of the optimization: $\mathrm{A}^{i\leq k} = \left[\mathrm{I}|\mathbf{0}\right]$.

After the point set registration is performed, the second step of the mesh registration consists of interpolating a dense displacement field for the entire MRI image using the transformed MRI mesh points Y'. One advantage of our interpolation scheme is that the TPS parameters w already obtained by the deformable registration can be employed to warp an arbitrary point from the original MRI space into the TRUS image. Incorporating Y and w as RGB textures, the warping can easily be performed directly on the GPU in the fragment shader. Note that such a mapping can be performed in both directions, i.e. from Y to Y' and vice versa, but the mapping is not bijective in the general case [7]. Because MRI and PET images are acquired simultaneously and reconstructed in the same coordinate system, all three modalities are now registered.

[3] Available online: `https://code.google.com/p/gmmreg/`

2.4 Image-based Biopsy Guidance

Finally, the mapping parameters obtained in the previous step are utilized to guide the urologist during the biopsy procedure. Assuming the patient has not moved in the meantime, the transformation ${}^{\text{frame}}\text{T}_{\text{chair}}$ containing the real-time tracking information of the US probe is used to interactively identify which part of the 3D TRUS volume is currently visible on the US machine. Then, corresponding MPRs (multi-planar reconstructions) of the MRI and PET images according to the deformable registration are rendered and presented to the urologist. A virtual biopsy needle guide, previously calibrated, indicates an approximate needle insertion path, as illustrated in Fig. 1. Two separate views are employed for successful navigation: While the sole MRI image provides anatomical context, a fused representation of gray-scale MRI and colored PET allows for precise targeting of suspicious lesions. Target biopsies are taken by manoeuvring the US probe such that the virtual biopsy guide aligns with the target site.

3 Results

In order to evaluate the performance of the presented method, we first examine the applicability of the biospsy guidance system on agar-gelatin phantoms mimicking the conditions in prostate biopsy interventions as closely as possible. Next, we analyze the performance of the individual components of our system, i.e. segmentation, registration, and image-based guidance, on 13 real patient datasets acquired in clinical routine.

3.1 Phantom Experiments

Based on the previous work of Dang et al. [4] for multi-modality phantoms, we used agar and gelatin to generate several prostate phantoms with suitable tissue contrast in both MRI and ultrasound. First, egg-shaped (roughly 50×30×30 mm) prostate glands consisting of 6 weight percent (wt%) gelatin, 3 wt% agar, and blue food coloring were cast. Into each gland, three lesions with a diameter of around 5 mm were positioned at varying locations during cooling. To ensure good contrast between normal prostate tissue and lesions in MRI, the latter were made with 12 wt% gelatin, 8 wt% agar and red food coloring. The different colors of gland and lesions allow to visually distinguish the tissue types in biopsy samples. The urethra was mimicked by an air-filled plastic tube. For each prostate, an artificial rectum (modeled during casting by a glass cylinder of around 35 mm in diameter)

Phantom	User	Lesion 1	Lesion 2	Lesion 3	Total
1	Urologist	1/1	1/1	1/1	3/3 (100%)
2	Non-med. expert	2/2	2/2	1/2	5/6 (83%)
3	Urologist	2/2	1/1	1/2	4/5 (80%)

Table 1 Results of prostate phantom biopsy samples (number of positive cores / total number of cores). All lesions were positively sampled at least once.

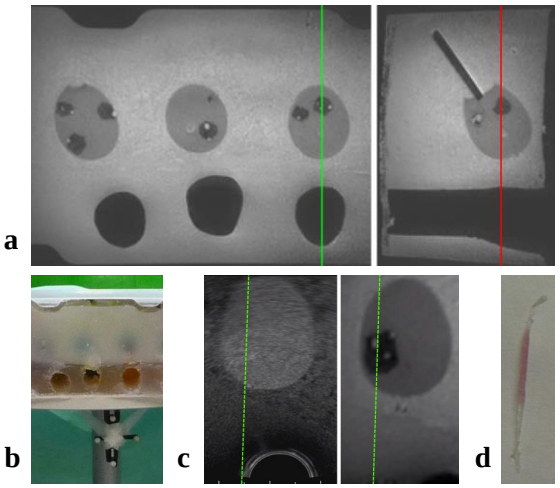

Fig. 3 a) Axial (left) and sagittal (right) MRI slices of agar-gelatin phantoms with lesions well visible. The vertical lines indicate the slice in the respective other view. **b)** Set-up for phantom biopsies with reference tracking target. **c)** Live TRUS image with invisible lesion and image-based MR guidance view during biopsy session. **d)** Positive core biopsy sample, lesion material visible due to red food color. *See text for details.*

was surrounded with a very elastic compound of 8 wt% gelatin and 1 wt% agar. Finally, the remaining phantom, now surrounding the prostate gland and maintaining a distance between rectal wall and gland of around 20 mm, was filled with a softer compound with only 1.8 wt% gelatin and 0.5 wt% agar. For efficiency, three prostate glands were positioned next to each other in one big plastic container and jointly MR-scanned, as illustrated in Fig. 3a-b. TRUS images were acquired following the procedure described in Sec. 2.1 for all three phantoms after two days. This time frame allowed diffusion between normal prostate tissue and lesions, making them almost invisible in ultrasound and thus mimicking real biopsy conditions well (cf. Fig. 3c). Due to the different intensity distributions compared to TRUS images of real patients, a semi-automatic segmentation approach [9] was employed for both TRUS and MRI, before the images were elastically registered as outlined in Sec. 2.3. Finally, an experienced urologist and a non-medical expert used the presented image-based guidance system to perform target biopsies. We considered a biopsy intervention on a particular phantom successful if all three lesions were hit at least once (visually identified using the red food color, cf. Fig. 3d), which was the case for all phantoms. In only 2 of 14 samples, the lesion was missed, possibly because of a different pressure of the transducer on the prostate compared to the initial TRUS image acquisition, leading to a distorted TRUS-MRI registration. Table 1 reports the biopsy samples in detail.

3.2 Patient Dataset and Protocol

For an evaluation of the segmentation and registration components as well as the validity of the entire system in clinical routine, a dataset of 13 patients was used. All of them underwent prostate biopsies without pathological finding in the past and were referred for a follow-up biopsy to our clinic. In preparation of the procedure for each patient, the prostate was carefully manually segmented in the MRI in order to perform the MRI-TRUS registration without user interaction during the intervention. After the acquisition of a 3D TRUS volume following the procedure

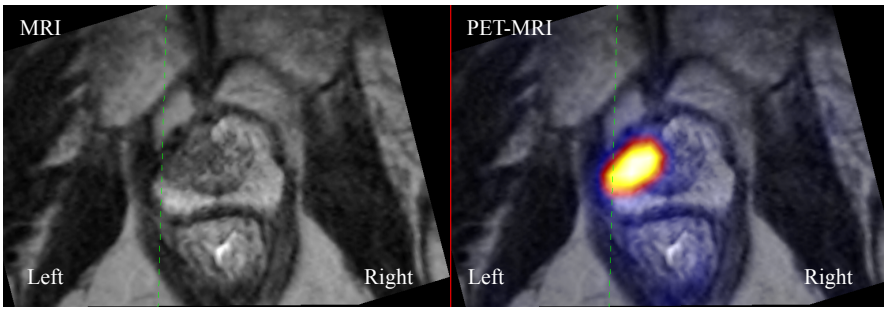

Fig. 4 The presented prostate biopsy guidance system provides the urologist with MRI and PET-MRI views corresponding to the current position of the TRUS transducer. The PET-MRI shows a hotspot in a suspicious region in left apical prostate zone where the target biopsies were taken. Note that because the urologist turns the transducer by 180° to take biopsies from the patient's left side (thus flipping the TRUS image), also the MRI and PET-MRI slices become flipped in our visualization.

outlined in Sec. 2.1, the prostate gland was automatically segmented and registered using the presented system. In total, less than five minutes were required from the end of the TRUS scan to the beginning of the biopsy procedure. In the following sections, segmentation and registration results are analyzed retrospectively. After the registration was performed, our system was used to guide targeted biopsies to suspicious areas identified in PET or MRI. In addition to the 12 regular biopsy cores spread throughout the prostate following the standard protocol, two targeted biopsy samples were taken from these areas. For five of these 13 cases, histology results are reported in Sec. 3.5. Figure 4 shows a screenshot of our image-based guidance system during a biopsy procedure, including the two MRI and PET-MRI views and the virtual needle guide lines.

3.3 Retrospective Evaluation of Prostate Segmentation

A dataset of 23 TRUS images, previously acquired in clinical routine following the procedure outlined in Sec. 2.1, was employed to train a Hough Forest, which was then used to automatically segment the prostate glands of the 13 patients during the biopsy session. For ground truth segmentations of both training and – retrospectively – testing images, manual expert annotations were used. As previously reported, e.g. by Reynier et al. [24], the segmentation of the basal and the apical parts of the prostate in US images is very challenging. Even to the human eye, delineating the boundaries in these regions is often ambivalent and will result in high intra- and inter-observer variability. In order to maintain comparability to ground truth segmentations, the prostate is subdivided into the three subregions *base*, *mid-gland* and *apex* following the convention in [21], i.e. according to 30%, 40% and 30% of the base-apex axis, respectively, and focus our evaluation on the *mid-gland* region only. As similarity metric, the surface distance between ground truth and the automatically obtained segmentations, as reported for all patients in Tab. 2, is used. Our method achieved an average surface distance of 1.04 ± 1.06 mm (mean $\pm$ standard deviation). The maximum distance between both surfaces was

Patient	Segmentation Surf. Dist.			TRE Rigid		TRE Deform.	
	Median	Mean	Std.Dev.	Mean	Max	Mean	Max
Pat. 1	0.56	0.98	1.09	1.14	1.45	0.94	1.45
Pat. 2	0.77	1.03	1.00	1.88	3.18	1.82	2.17
Pat. 3	0.41	0.62	0.67	1.92	2.96	0.88	1.12
Pat. 4	0.67	0.79	0.70	2.58	4.66	2.42	4.14
Pat. 5	2.16	2.69	2.37	3.62	5.62	1.74	2.70
Pat. 6	0.49	0.75	0.83	3.68	5.11	1.80	2.85
Pat. 7	0.86	1.14	1.13	2.38	2.79	2.80	3.73
Pat. 8	0.56	1.08	1.29	2.40	3.06	1.61	2.35
Pat. 9	0.41	0.66	0.76	2.19	3.96	3.55	6.56
Pat. 10	0.56	0.90	1.02	2.70	3.18	2.27	2.75
Pat. 11	0.62	0.81	0.77	1.82	2.00	1.79	2.35
Pat. 12	0.67	0.96	0.95	4.99	7.80	2.08	2.65
Pat. 13	0.77	1.13	1.18	2.60	3.60	2.27	3.64
Average	**0.73**	**1.04**	**1.06**	**2.60**		**2.00**	

Table 2 Segmentation and registration results for all patients. Segmentation results are reported as surface distances between ground truth and Hough forest-based segmentation [mm]. Registration results compare target registration errors (TRE) [mm] for rigid and automatic deformable registration, computed with four landmarks each. *See text for details.*

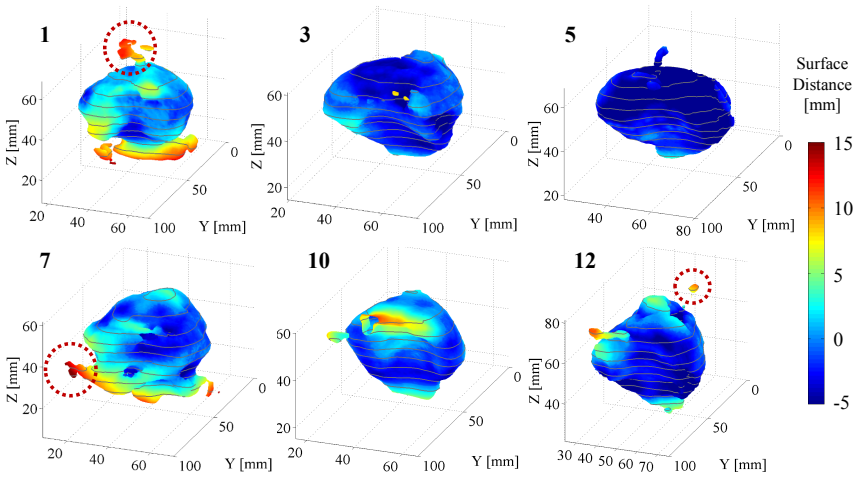

Fig. 5 Segmentation results for six representative patient datasets. The segmented surface indicates the distances to the ground truth segmentation according to the color bar on the right hand side. While segmentation artifacts extended far beyond the prostate in some datasets (dashed circles), the majority of the gland is segmented reasonably well. *Patient numbers coincide with the ones in Tab. 2. See text for details.*

on average 5.28 mm among all records. Segmentation results for six representative patient datasets are illustrated in Fig. 5, showing the triangulated segmentation surfaces as well as their color-coded distance to the ground truth annotation. As observed for instance for patients 1, 7, and 12, the algorithm produced in some cases artifacts stretching beyond the ground truth segmentation, having a clear impact on the surface distance. We also computed a Dice similarity score, which

was on average 87.81±2.92 for the *mid-gland* region, indicating potential for further improvements, also by using an extended and more diverse training dataset in the future. However, it has been previously shown that the registration algorithm is robust in terms of outliers and able to cope with such artifacts as long as the majority of the surface is appropriately well captured [18]. On our workstation, training using 23 datasets took approximately 105 min., and segmentation of the unseen dataset – without any optimization – around 3 min. depending on the size of the image.

3.4 Retrospective Evaluation of Prostate Registration

We evaluate the quality of the automatic registration, obtained using the automatic segmentation result from the previous step, by comparing it with rigid landmark-based registration. As in [25], four corresponding pairs of anatomical landmarks were carefully selected in MRI and TRUS for each patient, and rigid transformation matrices were obtained using the Umeyama method [30]. The experts performing these annotations were instructed to select landmarks from all parts of the gland such that the overall match would be optimal. In Fig. 6, rigid and deformable axial slice registration results are presented. In addition, we computed the target registration errors (TRE) for both methods and reported mean

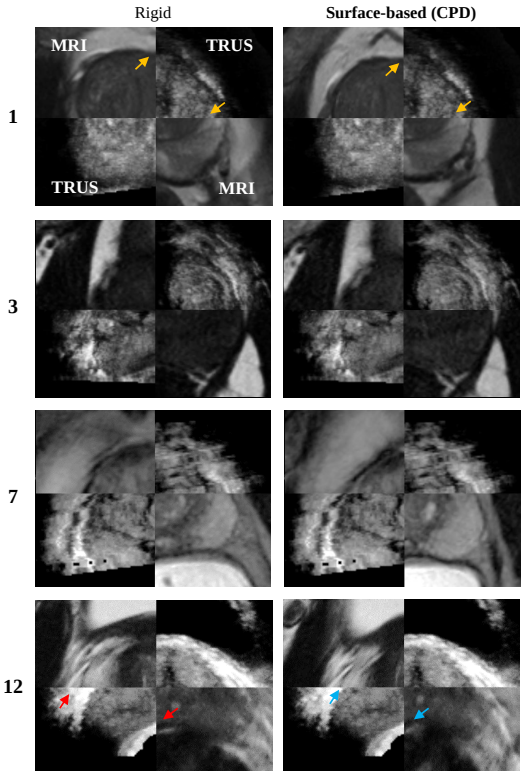

Fig. 6 Axial slice comparision between landmark-based rigid registration (*left column*) and deformable surface-based registration (*right column*) for four representative patients. In general, the deformable registration shows a good alignment between both images and captures the non-linear deformation better than in the rigid case. *Patient numbers coincide with the ones in Tab. 2. See text for details.*

Patient	PSA [ng/ml]	Suspicious Lesion	Random B.	Target B.	Gleason Sc.
1	9.8	left apical	3/12	1/1	3+4=7
4	10.0	right median basal	1/11	0/1	3+3=6
7	6.0	right central lateral	5/12	1/1	3+4=7
10	14.5	right median central	3/12	1/3	3+3=6
12	7.5	right central lateral	6/12	3/4	3+4=7

Table 3 Histology results for five cases are reported as number of positive cores / total number of cores for random and targeted biopsies, respectively. For all but one patient, at least one targeted sample was positive, indicating that the system is able to map suspicious lesions.

and maximum for each patient in Tab. 2. In some cases, little deformation was evident, resulting in low registration errors for both methods and good agreement of the fused images, for instance in patient 1 (*yellow arrows*). Severe deformations as seen in patient 12, however, were responsible for rigid landmark registration errors of up to 7.8 mm, causing significant misalignment of both images (*red arrows*). With our approach, a much better agreement between the surfaces was achieved (*blue arrows*), decreasing the mean TRE for this case from 5.0 to 2.1 mm. Overall, our method could improve the TRE in all but two cases, from an average 2.60 to 2.00 mm. In all cases, including these two, the TRE did not exceed 3.55 mm.

3.5 Clinical Histology Evaluation

As a detailed medical discussion of the findings for all patients would exceed the scope of this work, we present results for 5 patients where available histological evaluations indicated pathological findings. A full evaluation discussing the identification of suspicious lesions on PET/MRI and the detection rates of the biopsy guidance system will be the subject of a urological publication in preparation.

First, we report the PSA (Prostate-Specific Antigen) blood level prior to the biopsy and the location of the suspicious lesion identified in PET/MRI in Tab. 3. In addition, the number of positive and total biopsy cores for random and targeted biopsies, respectively, and the final Gleason score (standardized cancer grading system, grade of most common plus grade of next most common tumor pattern) are reported. In all cases, at least one of the targeted biopsy samples was positive, except for patient 4, where the only positive randomized biopsy core showed pathological findings in a different area than the targeted one. Our system was therefore able to successfully map suspicious regions from PET/MRI to the interventional TRUS image, and facilitated the diagnosis of prostate cancer. The application of the presented guidance system did not interrupt the established clinical procedure as the urologist could prepare the local anesthesia in the meantime.

4 Conclusion

In this work, we have presented a multimodal image-guided biopsy framework combining PET-MRI images with interventional TRUS. Our approach is based on an automatic segmentation of the prostate in the interventional TRUS image

using a Hough transform inspired machine learning technique, and the Coherent Point Drift algorithm, a surface-based, automatic deformable registration algorithm. We have individually evaluated both the segmentation and the registration algorithms and have presented results in the form of surface distance and landmark registration error, supporting the suitability of the method for the intended usage in both cases. As presented on a retrospective dataset of 13 patients, our system is robust in yielding smaller landmark registration errors compared to rigid registration. The proposed system was validated with phantom experiments and in a preliminary clinical evaluation with the help of urologists. Besides a broader clinical validation on a larger dataset, possible future extensions of our method include the use of an automatic approach for prostate segmentation in MRI to make the system fully automatic.

Acknowledgements and Remarks We thank Wolfgang Wein, ImFusion GmbH, for providing his image processing framework, and the teams of radiology and nuclear medicine departments at our clinic for various phantom MRI scans. This work is partially supported by the EU 7th Framework Program projects Marie Curie Early Initial Training Network Fellowship (PITN-GA-2011-289355-PicoSEC-MCNet), EndoTOFPET-US (GA-FP7/2007-2013-256984), and SoftwareCampus program of the German Federal Ministry of Education and Research (BMBF, Förderkennzeichen 01IS12057). The authors declare that they have no conflict of interest. Informed consent was obtained from all individual participants included in the study. All procedures performed in studies involving human participants were in accordance with the ethical standards of the institutional and national research committees.

References

1. Worldwide Cancer Key Facts 2014, Cancer Research UK. URL `http://publications.cancerresearchuk.org/downloads/Product/CS_KF_WORLDWIDE.pdf`
2. Cool, D.W., Bax, J., Romagnoli, C., Ward, A.D., Gardi, L., Karnik, V., Izawa, J., Chin, J., Fenster, A.: Fusion of MRI to 3D TRUS for mechanically-assisted targeted prostate biopsy: system design and initial clinical experience. In: Prostate Cancer Imaging. Image Analysis and Image-Guided Interventions, pp. 121–133. Springer (2011)
3. Criminisi, A., Shotton, J.: Decision forests for computer vision and medical image analysis. Springer (2013)
4. Dang, J., Frisch, B., Lasaygues, P., Zhang, D., Tavernier, S., Felix, N., Lecoq, P., Auffray, E., Varela, J., Mensah, S., Mingxi, W.: Development of an anthropomorphic breast phantom for combined pet, b-mode ultrasound and elastographic imaging. Nuclear Science, IEEE Transactions on **58**(3), 660–667 (2011)
5. Delongchamps, N.B., Peyromaure, M., Schull, A., Beuvon, F., Bouazza, N., Flam, T., Zerbib, M., Muradyan, N., Legman, P., Cornud, F.: Prebiopsy magnetic resonance imaging and prostate cancer detection: comparison of random and targeted biopsies. The Journal of urology **189**(2), 493–499 (2013)
6. Eiber, M., Nekolla, S.G., Maurer, T., Weirich, G., Wester, H.J., Schwaiger, M.: 68Ga-PSMA PET/MR with multimodality image analysis for primary prostate cancer. Abdominal imaging pp. 1–3 (2014)
7. Erikson, A.P., Åström, K.: On the bijectivity of thin-plate splines. In: Analysis for Science, Engineering and Beyond, pp. 93–141. Springer (2012)
8. Ghose, S., Oliver, A., Martí, R., Lladó, X., Vilanova, J.C., Freixenet, J., Mitra, J., Sidibé, D., Meriaudeau, F.: A survey of prostate segmentation methodologies in ultrasound, magnetic resonance and computed tomography images. Computer methods and programs in biomedicine **108**(1), 262–287 (2012)
9. Grady, L.: Random walks for image segmentation. IEEE Trans. Pattern Anal. Mach. Intell. **28**(11), 1768–1783 (2006)
10. Hu, Y., Ahmed, H.U., Taylor, Z., Allen, C., Emberton, M., Hawkes, D., Barratt, D.: MR to ultrasound registration for image-guided prostate interventions. Medical Image Analysis **16**(3), 687–703 (2012)

11. Jian, B., Vemuri, B.C.: Robust point set registration using Gaussian mixture models. IEEE Trans. Pattern Anal. Mach. Intell. **33**(8), 1633–1645 (2011)
12. Kaplan, I., Oldenburg, N.E., Meskell, P., Blake, M., Church, P., Holupka, E.J.: Real time MRI-ultrasound image guided stereotactic prostate biopsy. Magnetic resonance imaging **20**(3), 295–299 (2002)
13. Lasso, A., Heffter, T., Rankin, A., Pinter, C., Ungi, T., Fichtinger, G.: PLUS: Open-source toolkit for ultrasound-guided intervention systems. IEEE Transactions on Biomedical Engineering (10), 2527–2537 (2014)
14. Marks, L., Young, S., Natarajan, S.: MRI–ultrasound fusion for guidance of targeted prostate biopsy. Current opinion in urology **23**(1), 43 (2013)
15. Maurer, T., Beer, A.J., Wester, H.J., Kübler, H., Schwaiger, M., Eiber, M.: Positron emission tomography/magnetic resonance imaging with 68gallium-labeled ligand of prostate-specific membrane antigen: Promising novel option in prostate cancer imaging? International Journal of Urology (2014)
16. Milletari, F., Yigitsoy, M., Navab, N., Ahmadi, S.A.: Left ventricle segmentation in cardiac ultrasound using hough-forests with implicit shape and appearance priors. MIDAS Journal (2014)
17. Mitra, J., Kato, Z., Martí, R., Oliver, A., Lladó, X., Sidibé, D., Ghose, S., Vilanova, J.C., Comet, J., Meriaudeau, F.: A spline-based non-linear diffeomorphism for multimodal prostate registration. Medical Image Analysis **16**(6), 1259–1279 (2012)
18. Myronenko, A., Song, X.: Point set registration: Coherent point drift. IEEE Trans. Pattern Anal. Mach. Intell. **32**(12), 2262–2275 (2010)
19. Narayanan, R., Kurhanewicz, J., Shinohara, K., Crawford, E., Simoneau, A., Suri, J.S.: MRI-ultrasound registration for targeted prostate biopsy. In: Biomedical Imaging: From Nano to Macro, 2009. ISBI'09. IEEE International Symposium on, pp. 991–994 (2009)
20. Natarajan, S., Marks, L.S., Margolis, D.J., Huang, J., Macairan, M.L., Lieu, P., Fenster, A.: Clinical application of a 3d ultrasound-guided prostate biopsy system. In: Urologic Oncology: Seminars and Original Investigations, vol. 29, pp. 334–342. Elsevier (2011)
21. Qiu, W., Yuan, J., Ukwatta, E., Sun, Y., Rajchl, M., Fenster, A.: Prostate segmentation: An efficient convex optimization approach with axial symmetry using 3D TRUS and MR images. Medical Imaging, IEEE Transactions on (2014)
22. Reif, D.M., Motsinger, A.A., McKinney, B.A., Crowe, J.E., Moore, J.H.: Feature selection using a random forests classifier for the integrated analysis of multiple data types. In: Computational Intelligence and Bioinformatics and Computational Biology, 2006. CIBCB'06. 2006 IEEE Symposium on, pp. 1–8. IEEE (2006)
23. Rematas, K., Leibe, B.: Efficient object detection and segmentation with a cascaded Hough Forest ISM. In: Computer Vision Workshops (ICCV Workshops), 2011 IEEE International Conference on, pp. 966–973 (2011)
24. Reynier, C., Troccaz, J., Fourneret, P., Dusserre, A., Gay-Jeune, C., Descotes, J.L., Bolla, M., Giraud, J.Y.: MRI/TRUS data fusion for prostate brachytherapy. preliminary results. Medical physics **31**(6), 1568–1575 (2004)
25. Shah, A., Zettinig, O., Maurer, T., Precup, C., Schulte zu Berge, C., Weiss, J., Frisch, B., Navab, N.: An open source multimodal image-guided prostate biopsy framework. In: MICCAI Workshop on Clinical Image-based Procedures (CLIP). LNCS, vol. 8680. Springer (2014)
26. Sonn, G.A., Margolis, D.J., Marks, L.S.: Target detection: Magnetic resonance imaging-ultrasound fusion–guided prostate biopsy. In: Urologic Oncology: Seminars and Original Investigations. Elsevier (2013)
27. Sparks, R., Bloch, B.N., Feleppa, E., Barratt, D., Madabhushi, A.: Fully automated prostate magnetic resonance imaging and transrectal ultrasound fusion via a probabilistic registration metric. In: SPIE Medical Imaging, pp. 86,710A–86,710A. International Society for Optics and Photonics (2013)
28. Sperling, D.: MRI-ultrasound fusion imaging. In: Image Guided Prostate Cancer Treatments, pp. 115–123. Springer (2014)
29. Turkbey, B., Pinto, P.A., Choyke, P.L.: Imaging techniques for prostate cancer: implications for focal therapy. Nature Reviews Urology **6**(4), 191–203 (2009)
30. Umeyama, S.: Least-squares estimation of transformation parameters between two point patterns. IEEE Trans. Pattern Anal. Mach. Intell. **13**(4), 376–380 (1991)
31. Xu, S., Kruecker, J., Guion, P., Glossop, N., Neeman, Z., Choyke, P., Singh, A.K., Wood, B.J.: Closed-loop control in fused mr-trus image-guided prostate biopsy. In: MICCAI 2007. LNCS, pp. 128–135. Springer (2007)